Ursolic acid inhibits the proliferation of triple-negative breast cancer stem-like cells through NRF2-mediated ferroptosis

XINHUA YANG[1,2*], BEIBEI LIANG[3*], LISHA ZHANG[4], MINGZHU ZHANG[5], MING MA[2], LIJUAN QING[1], HAO YANG[3], GANG HUANG[3] and JIAN ZHAO[1-3]

[1]Graduate School, Shanghai University of Traditional Chinese Medicine, Shanghai 201203, P.R. China; [2]Shanghai Key Laboratory of Molecular Imaging, Shanghai University of Medicine and Health Sciences, Shanghai 201318, P.R. China; [3]Shanghai Key Laboratory of Molecular Imaging, Jiading Central Hospital Affiliated Shanghai University of Medicine and Health Sciences, Shanghai 201318, P.R. China; [4]The Preparation Center, Nanchang Hongdu Hospital of TCM, Nanchang, Jiangxi 330013, P.R. China; [5]School of Health Science and Engineering, University of Shanghai for Science and Technology, Shanghai 200093, P.R. China

Received February 6, 2024; Accepted May 22, 2024

DOI: 10.3892/or.2024.8753

Abstract. Ursolic acid (UA), a pentacyclic triterpenoid that has been found in a broad variety of fruits, spices and medicinal plants, has various biological effects such as reducing inflammation, protecting cells from damage, and preserving brain function. However, its impact on ferroptosis in cancer stem-like cells remains unexplored. The present study investigated the effect of UA on MDA-MB-231 and BT-549 cell-derived triple-negative breast CSCs (BCSCs) and its potential ferroptosis pathway. The effects of ferroptosis on BCSCs were demonstrated by the detection of ferroptosis-related indexes including the intracellular level of glutathione, malondialdehyde, reactive oxygen species and iron. The effects of UA on the biological behaviors of BCSCs were analyzed by Cell Counting Kit-8, stemness indexes detection and mammosphere formation assay. The mechanism of UA induction on BCSCs was explored by reverse transcription-quantitative PCR and western blotting. BALB/c-nude mice were subcutaneously injected with MDA-MB-231-derived BCSCs to establish xenograft models to detect the effects of UA *in vivo*. The results revealed that BCSCs have abnormal iron metabolism and are less susceptible to ferroptosis. UA effectively reduces the stemness traits and proliferation of BCSCs in spheroids and mice models by promoting ferroptosis. It was observed that UA stabilizes Kelch-like ECH-associated protein 1 and suppresses nuclear factor erythroid-related factor 2 (NRF2) activation. These findings suggested that the ability of UA to trigger ferroptosis through the inhibition of the NRF2 pathway could be a promising approach for treating BCSCs, potentially addressing metastasis and drug resistance in triple-negative breast cancer (TNBC). This expands the clinical applications of UA and provides a theoretical basis for its use in TNBC treatment.

Correspondence to: Professor Jian Zhao, Shanghai Key Laboratory of Molecular Imaging, Shanghai University of Medicine and Health Sciences, 279 Zhouzhu Road, Shanghai 201318, P.R. China
E-mail: j-zhao@vip.126.com

Professor Gang Huang, Shanghai Key Laboratory of Molecular Imaging, Jiading Central Hospital Affiliated Shanghai University of Medicine and Health Sciences, 1 Chengbei Road, Shanghai 201318, P.R. China
E-mail: huanggang@sumhs.edu.cn

*Contributed equally

Abbreviations: UA, ursolic acid; TNBC, triple-negative breast cancer; TNBCs, triple-negative breast cancer cells; CSCs, cancer stem-like cells; BCSCs, breast CSCs; PTX, paclitaxel; ROS, reactive oxygen species; GSH, glutathione; TF, transferrin; TFR1, TF receptor 1; FTH1, ferritin heavy chain 1; FPN, ferroportin; NRF2, nuclear factor erythroid-related factor 2; GPX4, glutathione peroxidase 4; SLC7A11, solute carrier family 7 member 11; FSP1, ferroptosis suppressor protein 1; KEAP1, Kelch-like ECH-associated protein 1; DFO, deferoxamine; ZVAD, Z-VAD-FMK; fer, ferrostatin-1; CQ, chloroquine; DMEM, Dulbecco's modified Eagle's medium; CCK-8, Cell Counting Kit-8; ALDH, aldehyde dehydrogenases; MDA, malondialdehyde; DMSO, dimethyl sulfoxide; NCOA4, nuclear receptor coactivator 4; p-NRF2, phosphorylated NRF2

Key words: UA, CSCs, TNBC, ferroptosis, NRF2 pathways

Introduction

Breast cancer stands out as the most prevalent malignant tumor affecting women worldwide, with its incidence and fatality rates escalating annually, as indicated by the 2020 Global Cancer Report from the International Agency for Research on Cancer of the World Health Organization (1). Recent global statistics revealed a staggering 2.26 million new cases of breast cancer, surpassing lung cancer for the first time to claim the top spot in worldwide incidence (2). Projections suggest a continued rise in incidence over the coming decades. Metastatic spread of cancer cells remains the primary cause of death in breast cancer cases (3). Triple-negative breast cancer

(TNBC), characterized by the absence of progesterone receptor, estrogen receptor and human epidermal growth factor receptor 2, represents a subtype associated with heightened metastasis, invasiveness and grim prognosis, constituting ~10-15% of all breast cancer cases (4). Notably, patients with distant metastases exhibit a dismal 5-year survival rate of merely 11.2% compared with non-triple-negative types (5). Chemotherapy remains the cornerstone of TNBC treatment due to its extensive heterogeneity and the absence of well-defined molecular targets (4).

Cancer stem-like cells (CSCs) comprise a small subset of malignant tumor cells possessing stem cell-like properties. Within TNBCs, there exists a notable enrichment of breast CSCs (BCSCs), characterized by their capacity for self-renewal, differentiation and generation of rapidly proliferating tumor cells, thus driving tumor progression and metastasis (6). Consequently, BCSCs are recognized as pivotal contributors to TNBC recurrence and metastasis (7). However, conventional chemotherapeutic agents such as Paclitaxel (PTX) often fail to eradicate BCSCs, thereby increasing the risk of recurrence (8). Therefore, there is an urgent need for novel agents targeting BCSCs to enhance the prognosis of patients with breast cancer.

Ferroptosis, a type of programmed cell death distinct from apoptosis and necrosis, was defined in 2012 (9). It is characterized by the accumulation of lipid peroxidation in the cell membrane and high levels of intracellular reactive oxygen species (ROS). This process involves four key biological processes: Glutathione (GSH) metabolism, iron metabolism, lipid metabolism and oxidative stress (10). Iron metabolism plays a critical role in maintaining the characteristics of CSCs (11). Ferric ions (Fe^{3+}) bind to transferrin (TF) or TF receptor 1 (TFR1) at the cell surface and are endocytosed into cells. In endosomes, Fe^{3+} is released and reduced to ferrous iron (Fe^{2+}). In the cytosol, Fe^{2+} ions constitute a labile intermediate pool. Free iron is stored in ferritin heavy chain 1 (FTH1) or exported by ferroportin (FPN). Ferric iron promotes cancer cell growth by activating the ribonucleotide reductase enzyme, while ferrous iron enhances lipoxygenase, promoting ferroptosis (12). CSCs predominantly store iron in the ferric state (ferritin), limiting the availability of ferrous iron and inhibiting ferroptosis (12). In breast cancer, CSCs exhibit higher expression levels of TFR1 and cellular iron compared with non-CSCs (13). Iron chelation abolishes the expression of CSC surface markers and stemness characteristics (14). Nuclear factor erythroid-related factor 2 (NRF2) is an oxidative-stress-responsive transcription factor that reduces ferroptosis by stimulating the expression of ferroptosis-suppressing genes, such as glutathione peroxidase 4 (GPX4), solute carrier family 7 member 11 (SLC7A11) and ferroptosis suppressor protein 1 (FSP1) (15). Under oxidative conditions, NRF2 is released from Kelch-like ECH-associated protein 1 (KEAP1) and translocated to the nucleus.

The exploration of targeted activation of ferroptosis as a means of treating CSCs holds promise in cancer therapy (16). Ursolic acid (UA) is a natural pentacyclic triterpenoid compound with diverse pharmacological activities against various cancer types (17). Recent studies have shown that UA can inhibit the growth of TNBC and has effects on metastasis and drug resistance (18,19). Additionally, UA has been found to inhibit the stemness characteristics of BCSCs (20). A recent study demonstrated that UA, when combined with sorafenib, can inhibit cancer cell growth by inducing apoptosis or SLC7A11-dependent ferroptosis (21). However, the precise effects of UA on the regulation of ferroptosis and its potential for targeting BCSCs to inhibit tumor growth remain largely unknown.

In the present study, spheroids of TNBC cells were treated and mice were xenografted with UA to explore the effects of UA on BCSCs and its underline mechanism.

Materials and methods

Chemicals and reagents. UA (cat. no. U6753) and deferoxamine (DFO; cat. no. D9533) were procured from Sigma-Aldrich; Merck KGaA. Z-VAD-FMK (ZVAD; cat. no. S7023) and ferrostatin-1 (fer; cat. no. S7243) were obtained from Selleck Chemicals. Chloroquine (CQ; cat. no. HY-17589A) and PTX (cat. no. HY-B0015) were purchased from MedChemExpress.

Cell culture. MDA-MB-231 and BT-549 cell lines were sourced from the Shanghai Institute of Biotechnology, Chinese Academy of Science. Cell line expansion and cryopreservation followed the guidelines of the American Pharmacopoeia Commission, with periodic mycobacterial inspection. MDA-MB-231 cells were cultured in Dulbecco's modified Eagle's medium (DMEM) (HyClone; Cytiva), while BT-549 cells were cultured in Roswell Park Memorial Institute-1640 media (HyClone; Cytiva). Both cell lines were supplemented with 10% fetal bovine serum (Bioexplorer, Inc.) and maintained in a humid environment with 5% CO_2 at 37˚C. Subsequently, cells were kept under stem cell conditions using serum-free DMEM/F12 (Gibco; Thermo Fisher Scientific, Inc.) supplemented with 10 ng/ml human recombinant epidermal growth factor (EGF) (Invitrogen; Thermo Fisher Scientific, Inc.). Adherent cells of MDA-MB-231 and BT-549 were seeded into ultra-low attachment 6-well plates (Corning, Inc.) to form non-adherent spheroids at a density of $8x10^4$ cells/well, with medium replacement every four days.

Fluorescence-activated cell sorter analysis for CD44/CD24 cells. Non-adherent spheroids were stained with CD44-APC (cat. no. 397517; BioLegend, Inc.), CD24-FITC (cat. no. 311117; BioLegend, Inc.) and respective isotype controls. After a 40-min incubation in the dark, cells were detected using the NovoCyte flow cytometer (ACEA Bioscience, Inc.) and analyzed by NovoExpress 1.5.8 software (Agilent Technologies, Inc.).

$CD44^+/CD24^-$ cells isolation. The manufacturer's protocol for the CD24 Microbead Kit (cat. no. 130-095-951; Miltenyi Biotec GmbH) was adhered to for the cultivation of $3x10^7$ MDA-MB-231 and BT-549 mammospheres using a primary antibody against CD24. Subsequently, the labeled cells were incubated with IgG microbeads (Miltenyi Biotec GmbH) and underwent magnetic separation using MiniMACS columns (Miltenyi Biotec GmbH). The purified $CD24^-$ cells were then incubated with CD44 microbeads (cat. no. 130-095-194; Miltenyi Biotec GmbH), washed and subjected to magnetic separation once more.

Cell viability assay. Cellular proliferation was monitored according to the manufacturer's protocol using an optical microscope and quantitatively assessed via the Cell Counting Kit-8 (CCK-8) assay (Chongqing Baoguang Biotech Co., Ltd.; http://www.bgbiotech.com/) across various experimental groups. MDA-MB-231 and BT-549 adherent cells and spheroids were seeded into 96-well microplates or ultra-low attachment 96-well plates at a density of $1x10^4$ cells per well. After incubation at 37˚C for 24 h, cells were treated with varying concentrations of UA or PTX (0, 10, 20, 40 μM) for 24 h, respectively. Subsequently, 10 μl of CCK-8 reagent was added per well, and the plates were incubated for 2 h. Cell viability was determined using the formula: Cell viability (%)=[(As-Ab)/(Ac-Ab)]x100%, where Ab, As, and Ac respectively denote the absorbance values at 450 nm wavelength for the blank medium, experimental group and control group.

Aldehyde dehydrogenase (ALDH) activity assay. The ALDH assay kit (cat. no. MAK082; Sigma-Aldrich; Merck KGaA) was employed for assessing ALDH activity, using $1x10^6$ cells per group. The colorimetric product measured at 450 nm was directly proportional to the ALDH activity present. The experiments were repeated at least three times.

ROS assay. The ROS assay kit (cat. no. S0033S; Beyotime Institute of Biotechnology) was utilized. Cells were seeded at a density of $5x10^4$ cells per well in either a standard 24-well plate or an ultra-low attachment 24-well plate. Intracellular ROS were measured using the DCFH-DA probe. Images of randomly selected fields were captured using a fluorescence microscope. The experiments were repeated at least three times.

GSH and malondialdehyde (MDA) assay. The GSH (cat. no. KTB1600) and MDA (cat. no. KTB1050) assay kits were obtained from Abbkine Scientific Co., Ltd. The relative contents of MDA and GSH were detected following the manufacturer's recommended protocol. Each group prepared $1x10^6$ cells. The GSH and MDA levels of each group were determined by spectrophotometer detection at 412, 532 and 600 nm. The experiments were repeated at least three times.

Iron assay. The iron assay kit (cat. no. ab83366) was supplied by Abcam. In a physiological context, Fe^{2+} reacts with the iron probe to form a stable colored complex exhibiting absorbance at 593 nm. Additionally, Fe^{3+} can be reduced to Fe^{2+}, enabling the accurate measurement of total iron (both Fe^{2+} and Fe^{3+}) by adding iron reducer. The concentration of Fe^{3+} was determined by subtracting the Fe^{2+} content from the total iron level. To assess the iron content, $2x10^6$ cells were collected from each experimental group. The experiments were repeated at least three times.

Western blotting (WB). Primary antibodies against CD44 (1:1,000; cat. no. ab189524), CD24 (1:1,000; cat. no. ab179821), TFR1 (1:1,000; cat. no. ab214039), KEAP1 (1:1,000; cat. no. 10503-2-ap) and LaminB1 (1:1,000; cat. no. 10503-2-ap) were supplied by Abcam, while the phosphorylated (p-) NRF2 (1:1,000; cat. no. ap1133) antibody was supplied by ABclonal Biotech Co., Ltd. and NRF2 (1:1,000; cat. no. 12721s) was bought from Cell Signaling Technology, Inc. Total protein was extracted from cells or tissues of each sample group using WB and IP cell lysates. Quantification was achieved using the BCA Protein Assay kit (cat. no. 23227; Thermo Fisher Scientific, Inc.). Subsequently, protein samples (20 micrograms per well) were separated by SDS-PAGE on a 10% gel and transferred onto PVDF membranes via electrophoresis. The membranes were blocked with blocking buffer (Vazyme Biotech Co., Ltd.) for 30 min at room temperature, followed by overnight incubation with primary antibodies at 4˚C. The next day, the membranes were incubated with HRP-conjugated anti-rabbit secondary antibodies (1:10,000; cat. no. ab6721; Abcam) for 1 h at room temperature. The target protein was then detected by exposure to an ECL luminescent solution (Shanghai Yeasen Biotechnology Co., Ltd.). Quantitative protein analysis was performed using ImageJ 1.8.0 software (National Institutes of Health).

Preparation of protein extractions. The Nuclear Extract Kit (cat. no. 40010) was purchased from Active Motif, Inc. MDA-MB-231 spheroids were plated in an ultra-low attachment dish (100 mm) at a density of $5x10^6$ cells/well and incubated for 4 h. The cells were then treated with 20 μM UA, 2 μM fer, or 10 μM DFO for 48 h. After washing the cells twice with ice-cold PBS containing phosphatase inhibitors, the cells were harvested by scraping the wells. The harvested suspension was centrifuged at 200 x g at 4˚C for 5 min. To extract nuclear protein, the cell pellets were initially treated with hypotonic buffer for 15 min and then centrifuged at 14,000 x g at 4˚C for 30 sec. The supernatants, representing the cytosolic fractions, were discarded. The pellets, designated as nuclear fractions, were lysed again in Complete Lysis Buffer (Active Motif, Inc.). The cell lysates were vortexed every 5 min for a total of 30 min and then centrifuged at 14,000 x g at 4˚C for 10 min. The supernatants were isolated and collected as the nuclear protein extract.

RNA extraction and reverse transcription-quantitative polymerase chain reaction (RT-qPCR) analysis. Total RNA was isolated from MDA-MB-231 and BT-549 cells, as well as their respective sphere cells, using the Tissue RNA Miniprep Kit (cat. no. BW-R6311; Biomiga, Inc.). According to the manufacturer's instructions, a total of 500 ng of total RNA from each sample was used for the reverse transcription reaction using the HiScript III RT SuperMix (+gDNA wiper) (cat. no. R323-01; Vazyme Biotech Co., Ltd.). qPCR was performed on cDNA templates using ChamQ SYBR Color qPCR Master Mix (cat. no. Q431-02; Vazyme Biotech Co., Ltd.) on a realplex RT-qPCR system (Eppendorf SE). All qPCR reactions were conducted in a total volume of 10 μl. The qPCR protocol started with an initial denaturation step at 95˚C for 5 min, followed by 40 amplification cycles, each consisting of denaturation at 95˚C for 30 sec, annealing at 60˚C for 30 sec, and extension at 72˚C for 30 sec. The primer sequences used for the analysis of each gene are comprehensively listed in Table SI.

Mammosphere formation. Single cell suspensions of MDA-MB-231 and BT-549 spheroids were prepared by pipetting. In DMEM/F-12 medium supplemented with 20 ng/ml EGF and 10% B27, the single cell suspensions were cultured

in ultra-low adhesion 6-well plates at a density of $2x10^4$ cells per well to generate mammospheres for 7 days. A total of 3-5 randomly selected fields of view per well were counted, and floating aggregates >50 μm in diameter were chosen as mammospheres for further analysis. The total mammosphere area was used for statistical analysis.

In vivo xenograft experiments. Female Balb/C mice, aged 5 weeks and weighing between 16-18 grams, were obtained from Shanghai Jihui Laboratory Animal Care Co., Ltd. The mice were housed in specific pathogen-free conditions with 24-26˚C temperature, 50-60% humidity and 12/12-h light/dark cycle at the Animal Resource Center of the Shanghai University of Medicine and Health Sciences, where they were provided with autoclaved water and food *ad libitum*. The efficacy of UA *in vivo* was assessed using an MDA-MB-231 spheroid xenograft model. Animals underwent a one-week acclimatization period before being used in experiments. Dissociated MDA-MB-231 spheroids ($5x10^6$) were resuspended in 100 μl PBS and injected subcutaneously into the right flank of mice. Engrafted mice were monitored for tumor development through visual inspection until tumor formation occurred. On the 14th day post-injection, the mice were randomly assigned to 7 treatment groups, with 5 mice per group. Mice received intraperitoneal injections of 30 μl 10% dimethyl sulfoxide (DMSO) (22-24), which was freshly diluted in a saline containing 0.9% NaCl, containing UA (20 mg/kg body weight, daily) (25), or PTX (20 mg/kg body weight, daily) (26), or together with fer (5 mg/kg body weight, daily) (27) or DFO (100 mg/kg body weight, daily) (28) for 30 days. Body weight, tumor mass and the health indexes of mice (strong appetite, bright eyes, quick reaction, power of muscles) were assessed every 5 days. Tumor volume was measured using Vernier calipers and calculated using the following formula: $Width^2$ x length x $\pi/6$. According to the Laboratory animal Guidelines for euthanasia in China, the criteria used to determine when animals should be euthanized included: i) The maximum tumor diameter approaching 15 mm; ii) loss of weight >20%; iii) difficulty to move or breath. When the maximum tumor diameter approached 15 mm (the 30th day of treatment), mice were administered 2.5% isoflurane for induction of anesthesia by inhalation for 3 min and then 1.5% isoflurane for maintenance of anesthesia before being euthanized. Mice were euthanized by cervical dislocation under anesthesia to ensure humane conditions for the study. The mice were observed to have no response, including limb paralysis and no rise and fall of the chest to confirm death. The duration of the *in vivo* experiment was 44 days totally, including 14 days for tumor cells to proliferate *in vivo* and 30 days for the treatment with individual drug. Totally, 35 mice were used in the present study with no mice succumbing before the end of study.

Immunohistochemistry (IHC) staining. The expression of KEAP1, NRF2 and TFR1 in cancer tissues was assessed using IHC staining. The tumors were fixed with 4% paraformaldehyde overnight at 4˚C and then embedded in paraffin. Paraffin sections (4-6 μm) were heated in an oven at 60˚C for 60 min and then dehydrated in xylene, followed by a series of ethanol washes (anhydrous ethanol, 95, 85 and 75% ethanol). Subsequently, the slices underwent three consecutive washes with PBS. Antigen retrieval was performed in sodium citrate buffer solution at 120˚C for 15 min. After blocking with goat serum (cat. no. 16210064; Gibco; Thermo Fisher Scientific, Inc.) for 10 min at room temperature, the sections were incubated with primary antibodies against KEAP1 (1:500), NRF2 (1:500) and TFR1 (1:350) overnight at 4˚C. The following day, the slices were washed with PBS and then incubated with biotin-labeled goat anti-rabbit antibody (1:1,000; cat. no. R-21234; Invitrogen; Thermo Fisher Scientific, Inc.) at 37˚C for 1 h. DAB solution was applied to stain the samples, followed by counterstaining with hematoxylin at room temperature for 3 min. Finally, images were captured using a light microscope and quantitatively analyzed by IHC mean optical density (MOD) values. MOD value=(staining intensity x staining area)/total tissue area.

Statistical analysis. All data were presented as the mean ± SD from three independent experimental replicates. Comparison between two groups was performed using unpaired t-test. Statistical analysis of multiple groups was performed using one-way analysis of variance with Tukey's post hoc test using GraphPad Prism 9.0 (GraphPad Software; Dotmatics). $P<0.05$ was considered to indicate a statistically significant difference.

Results

BCSCs exhibit less lipid peroxidation. BCSCs, enriched through the formation of non-adherent spheroids, exhibit characteristics of CSCs (29). $CD44^+/CD24^-$ cells and $ALDH^{high}$ cells are widely recognized as BCSCs (30). In the present study, BCSCs were collected from MDA-MB-231 and BT-549 cells within non-adherent spheroids, showing higher CD44 expression and lower CD24 expression compared with adherent cells, as detected by flow cytometric assay (Fig. 1A) and WB (Fig. 1B). ALDH activity was significantly elevated in spheroids compared with adherent cells (Fig. 1C). Moreover, the expression levels of putative stemness-associated markers CD133, EpCAM and transcription factors OCT4, Sox2 and c-myc were increased in spheroids (Fig. 1D). To further purify the CSCs, $CD44^+/CD24^-$ cells were isolated from MDA-MB-231 and BT-549 mammospheres using magnetic-activated cell sorting (Fig. S1). The intracellular ROS levels were slightly increased in spheroids and $CD44^+/CD24^-$ CSCs with no significant difference compared with adherent cells (Fig. 1E). Additionally, the amount of GSH, an intracellular antioxidant, was significantly higher in spheroids and $CD44^+/CD24^-$ CSCs than in adherent cells (Fig. 1F). However, lipid peroxidation levels were increased in $CD44^+/CD24^-$ CSCs compared with adherent cells, as evidenced by the amount of MDA in these cells (Fig. 1G). These findings suggested that BCSCs may possess a protective mechanism against lipid peroxidation.

BCSCs undergo less ferroptosis. Given that lipid peroxidation leads to ferroptosis, an iron-dependent form of cell death, several key regulators of ferroptosis were examined. Inhibitors of ferroptosis such as SLC7A11, GPX4 and NRF2 were significantly upregulated in spheroids and CSCs compared with adherent cells (Fig. 2A), indicating that BCSCs undergo less ferroptosis. Importantly, spheroids and CSCs exhibited enhanced iron uptake with higher TFR1 expression,

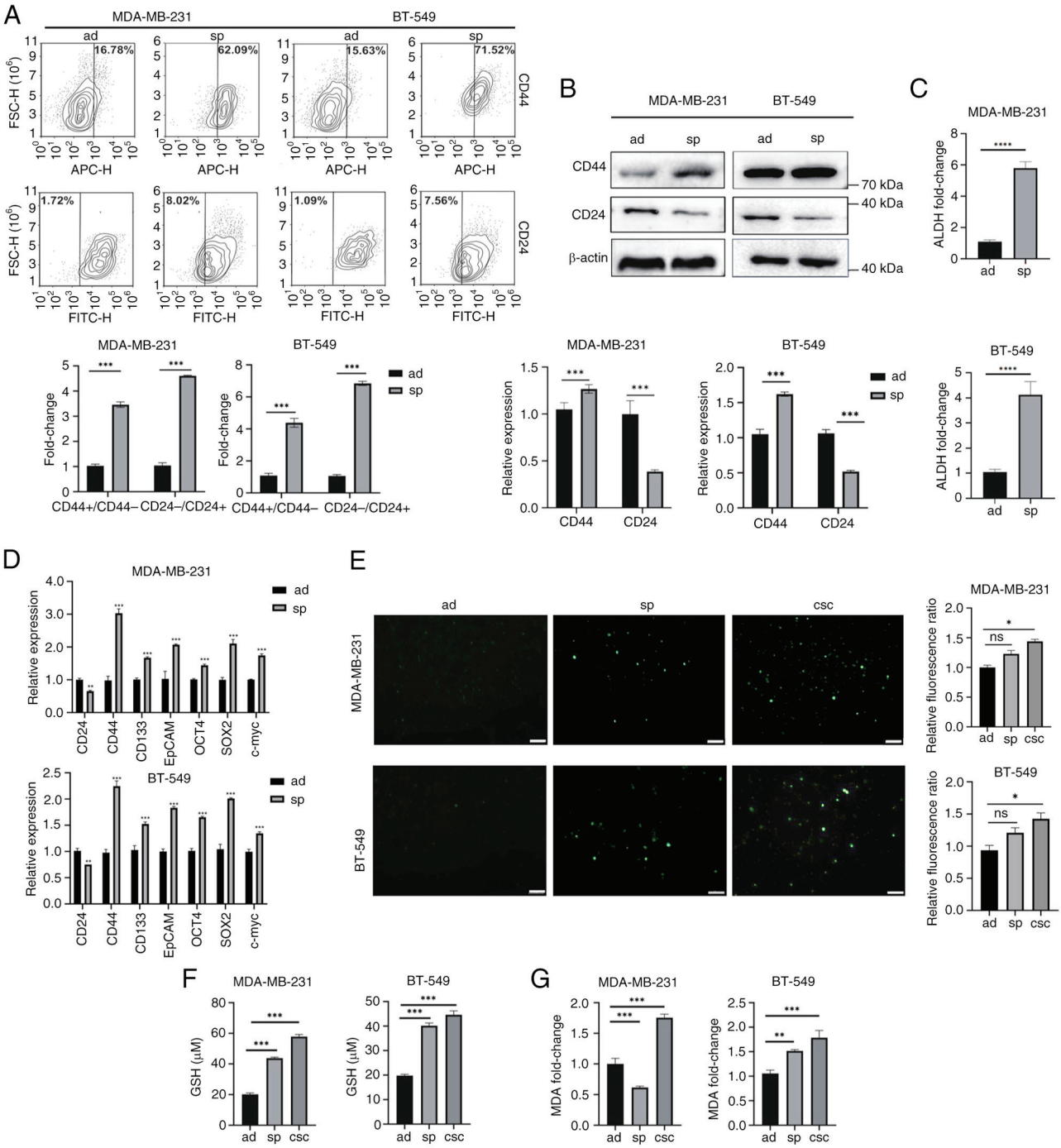

Figure 1. Breast cancer stem-like cells exhibit stemness characteristics and less lipid peroxidation. (A) MDA-MB-231 and BT-549 cells cultured in sp or ad cells were analyzed for CD44 and CD24 expression using flow cytometry. (B) Protein expression levels of CD24 and CD44 in ad cells and sp were detected by western blotting. All protein expression data were normalized relative to β-actin as a loading control. (C) Detection of ALDH enzyme activity in ad cells and sp. (D) The mRNA level of stemness-related genes in ad cells and sp were analyzed by reverse transcription-quantitative PCR. (E-G) Relative levels of reactive oxygen species, GSH and MDA in ad cells, sp and $CD44^+/CD24^-$ CSCs were measured by commercial assay kits. $^*P<0.05$, $^{**}P<0.01$, $^{***}P<0.001$ and $^{****}P<0.0001$. Scale bar, 100 μm. sp, spheroids; ad, adherent; ALDH, aldehyde dehydrogenase; GSH, glutathione; MDA, malondialdehyde; CSCs, cancer stem cells; ns, not significant (P>0.05).

increased iron storage with higher FTH1 expression, and reduced iron export with lower FPN expression (Fig. 2A). The expression of TFR1 was confirmed by WB (Fig. 2B). Indeed, spheroids and CSCs showed evident iron accumulation in ferric form (Fig. 2C). Conversely, ferrous iron, an activator of ferroptosis, was significantly lower in spheroids and CSCs compared with adherent cells (Fig. 2C). Thus, it was indicated that BCSCs might employ a protective mechanism against ferroptosis to maintain their stemness characteristics in an iron homeostasis-related manner.

UA inhibits breast cancer stem-like cell stemness characteristics and proliferation through inducing ferroptosis. Since BCSCs exhibit resistance to traditional chemotherapy drugs such as PTX, there is an urgent need to develop novel drugs targeting BCSCs. UA has gained

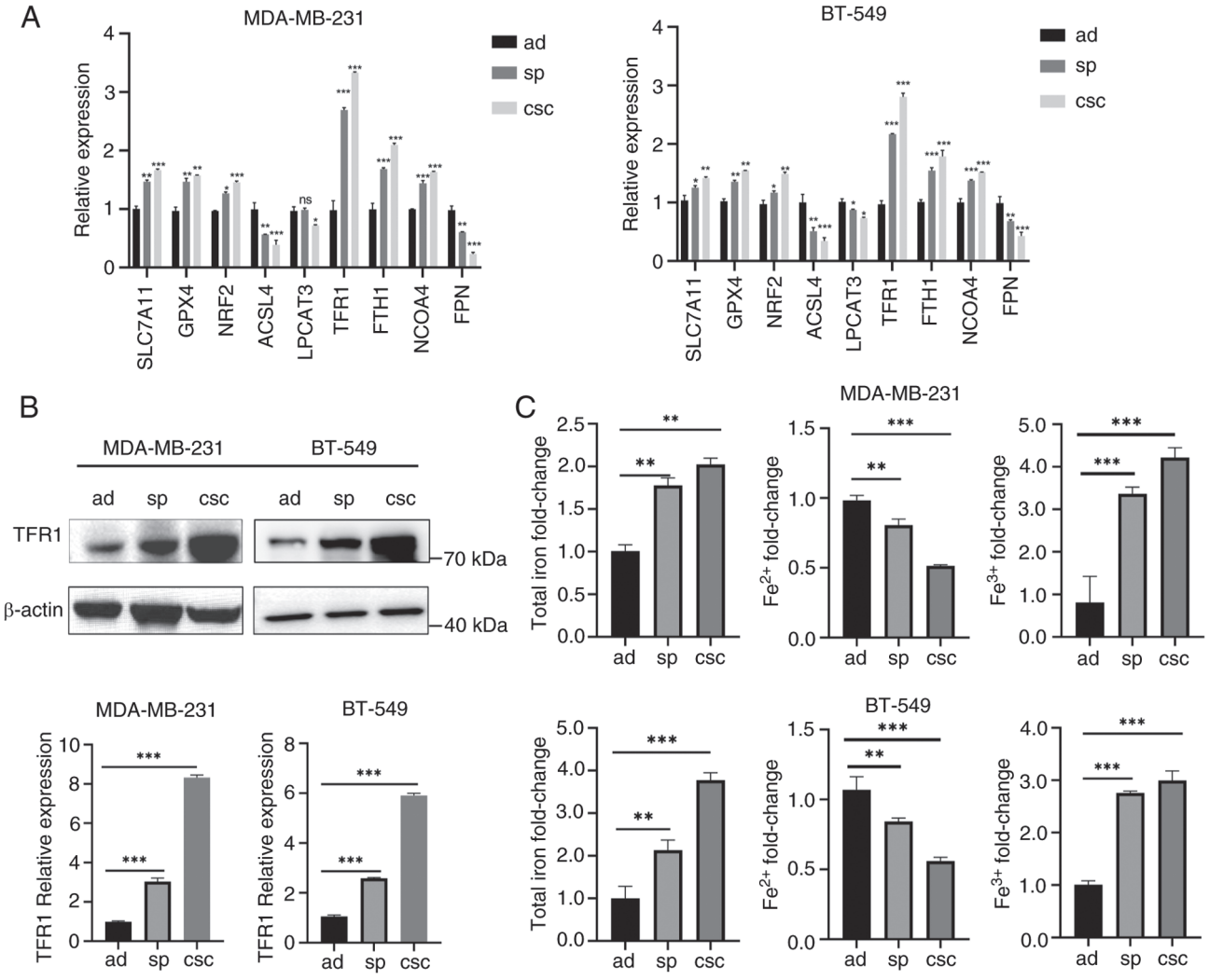

Figure 2. Breast cancer stem-like cells undergo less ferroptosis. (A) The mRNA levels of genes involved in ferroptosis were measured in MDA-MB-231 and BT-549 ad cells, sp and $CD44^+/CD24^-$ CSCs by reverse transcription-quantitative PCR. (B) Protein expression levels of TFR1 in MDA-MB-231 and BT-549 ad cells, sp and CSCs were detected by western blotting. (C) The contents of total iron, Fe^{2+}, and Fe^{3+} in MDA-MB-231 and BT-549 ad cells, sp and $CD44^+/CD24^-$ CSCs were measured by commercial assay kits. $^*P<0.05$, $^{**}P<0.01$ and $^{***}P<0.001$. ad, adherent; sp, spheroids; CSCs, cancer stem cells; TFR1, transferrin receptor 1; SLC7A11, solute carrier family 7 member 11; GPX4, glutathione peroxidase 4; NRF2, nuclear factor erythroid-related factor 2; NCOA4, nuclear receptor coactivator 4; FPN, ferroportin; ns, not significant (P>0.05).

attention as a potent anticancer agent in various cancers through inducing apoptosis or ferroptosis (27,31). However, whether UA could target CSCs by overcoming ferroptosis resistance remains unclear. In the present study, it was found that PTX and UA had no significant difference in inhibiting cell proliferation in adherent cells (Fig. 3A). However, breast cancer cell spheroids were more sensitive to UA-induced cell death than to PTX-induced cell death (Fig. 3A), indicating that UA is more effective than PTX in inducing cell death in BCSCs. Since the IC_{50} of UA on MDA-MB-231 and BT-549 spheroids was 25.8 and 18.6 μM, respectively (Fig. S2A and B), 20 μM of UA were then used for the treatment of breast cancer cells. To elucidate the mechanisms by which UA induces cell death in BCSCs, several cell death inhibitors were added. As demonstrated in Fig. 3B, the caspase inhibitor ZVAD failed to reverse UA-induced cell death in BCSCs. The autophagy inhibitor CQ efficiently reversed UA-induced cell death in BCSCs. Importantly, ferroptosis inhibitors fer (which blocks lipid peroxidation) and DFO (an iron chelator) significantly reversed UA-induced cell death in BCSCs. Thus, UA might induce cell death in BCSCs mainly through ferroptosis. Furthermore, mammosphere formation, a typical property of CSCs *in vitro*, was investigated upon UA treatment. UA significantly reduced the sphere formation ability of BCSCs (Fig. 3C). Fer and DFO significantly reversed the inhibitory effect of UA. The expression of stemness markers, CD44 and CD24, was also analyzed in BCSCs upon UA treatment. UA treatment led to a decrease in CD44 and an increase in CD24 in BCSCs, which could be reversed by fer and DFO (Fig. 3D). The stemness regulators OCT4, SOX2 and c-myc were downregulated by UA, which could be partly reversed by fer (Fig. 3E). These data indicated that UA efficiently inhibits stemness characteristics and proliferation of BCSCs through ferroptosis-related cell death.

UA induces ferrous iron and ROS accumulation in BCSCs. To further confirm ferroptosis induced by UA in BCSCs, intracellular ROS levels, lipid peroxidation levels and

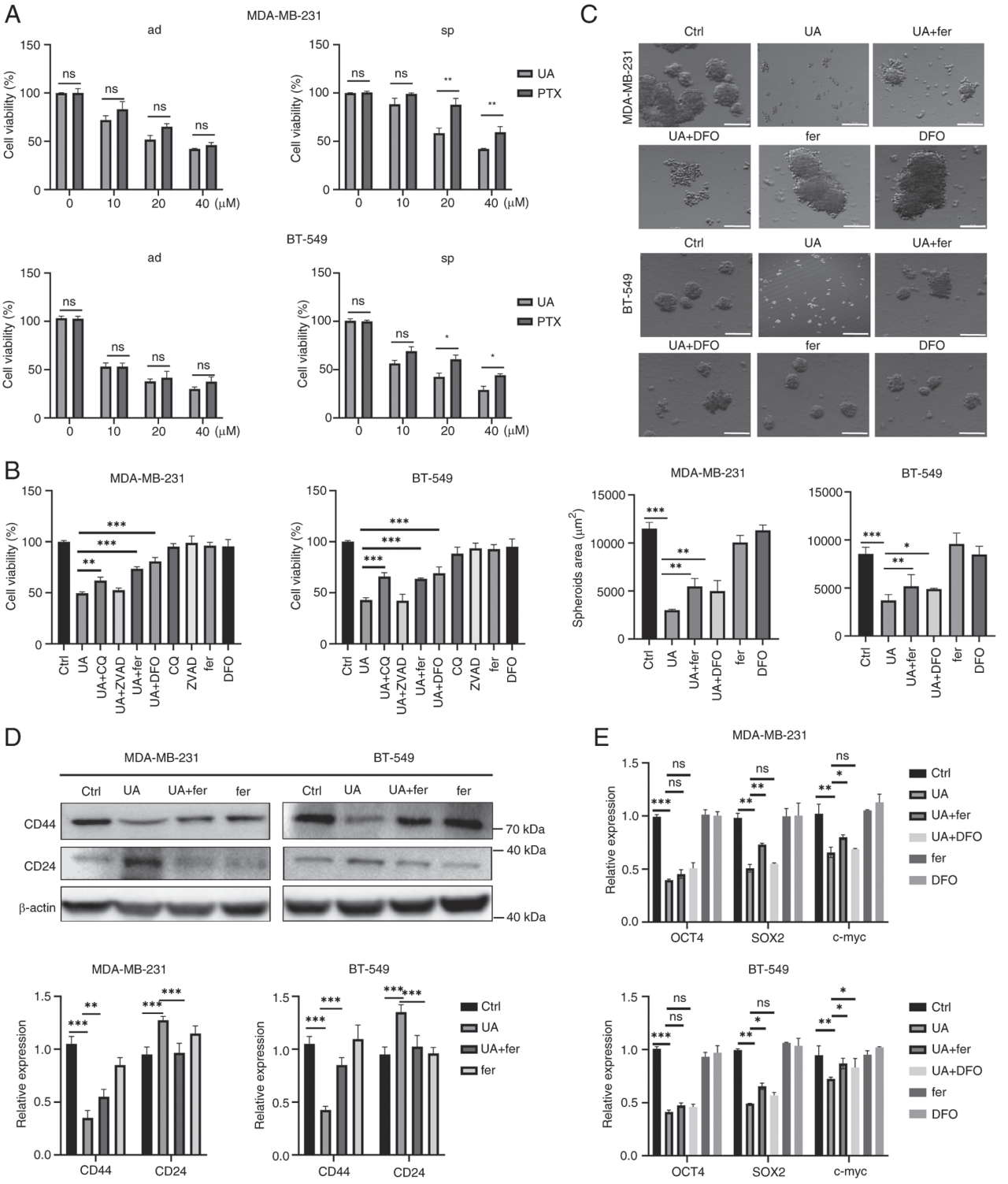

Figure 3. UA inhibits breast cancer stem-like cells stemness characteristics and proliferation through inducing ferroptosis. (A) Effect of UA or PTX on the cellular proliferation of MDA-MB-231 and BT-549 ad cells and sp using Cell Counting Kit-8 assay. Cells were treated for 24 h at varying concentrations (0, 10, 20, 40 μM). (B) Effects of different death pathway inhibitors on MDA-MB-231 and BT-549 sp. Cells were treated with UA (20 μM), ZVAD (10 μM), CQ (10 μM), fer (2 μM) or DFO (10 μM), respectively, or with combination as indicated for 24 h. (C) Representative images of mammospheres treated by UA (20 μM) with or without fer (2 μM) or DFO (10 μM) in sp for 24 h. (D) Protein expression levels of CD24 and CD44 in sp were detected by western blotting after the treatment of UA and fer for 24 h. (E) The mRNA levels of stemness-related genes in sp were analyzed by reverse transcription-quantitative PCR after the treatment of UA and fer for 24 h. *P<0.05, **P<0.01 and ***P<0.001. Scale bar, 100 μm. UA, ursolic acid; PTX, paclitaxel; ad, adherent; sp, spheroids; ZVAD, ZVAD, Z-VAD-FMK; CQ, chloroquine; DFO, deferoxamine; fer, ferrostatin-1; ns, not significant (P>0.05).

the amount of iron were detected. UA treatment led to a prominent increase in intracellular ROS in BCSCs (Fig. 4A). The UA-induced ROS eruption in BCSCs was significantly attenuated by fer and DFO (Fig. 4A). Lipid peroxidation levels, as indicated by the amount of MDA, were significantly enhanced in UA-treated BCSCs, which were alleviated by

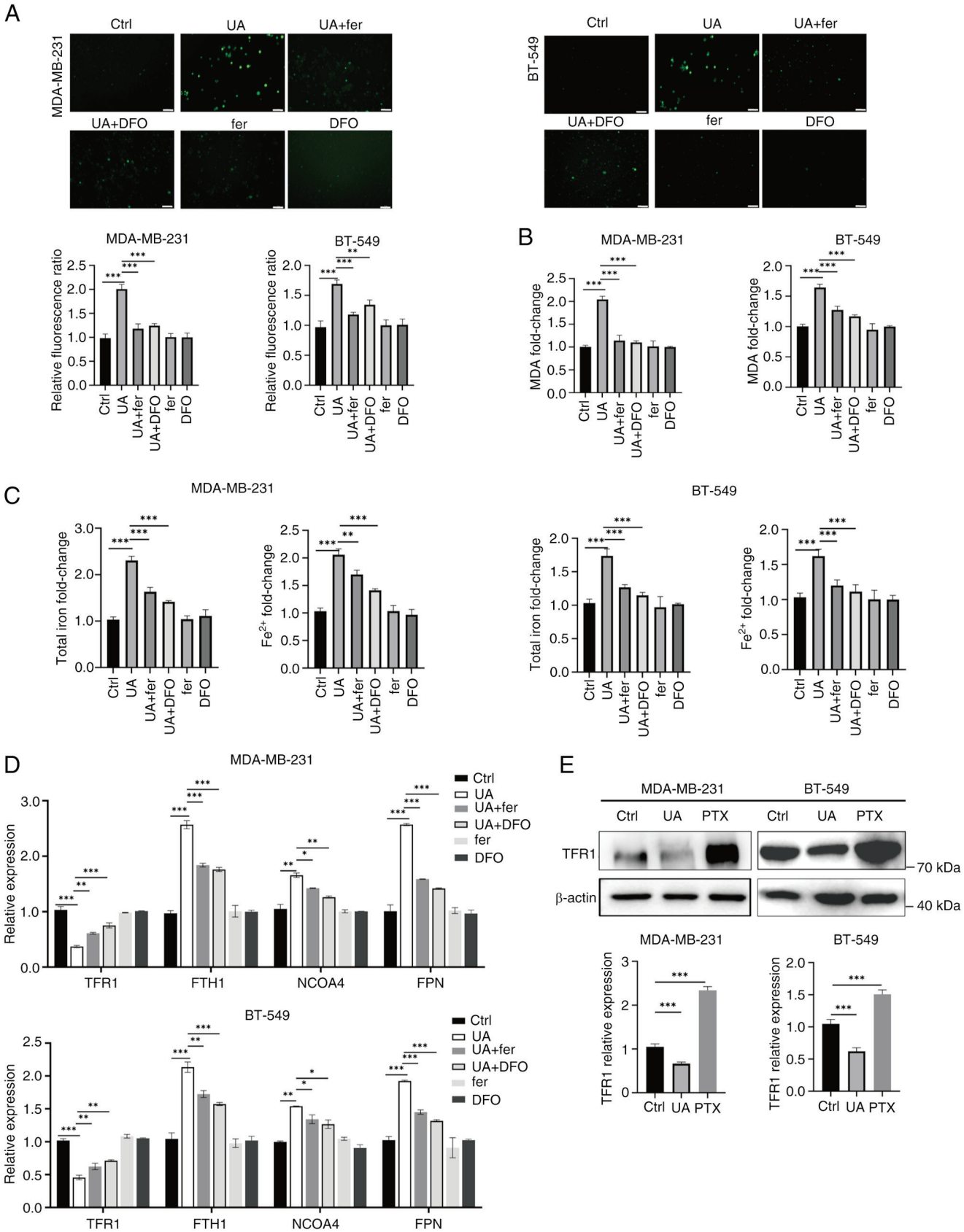

Figure 4. UA induces ferrous iron and ROS accumulation in breast cancer stem-like cells. (A) Fluorescence imaging of ROS (green) in MDA-MB-231 and BT-549 spheroids treated with UA (20 μM) together with or without ferroptosis inhibitors, fer (2 μM) and DFO (10 μM) for 24 h. (B and C) Relative levels of MDA, total iron and Fe^{2+} in spheroids were measured by commercial assay kits after the same treatment as in panel A. (D) The mRNA levels of iron metabolism-related genes TFR1, FTH1, NCOA4 and FPN in spheroids were analyzed by reverse transcription-quantitative PCR after the same treatment as in panel A. (E) Protein expression of TFR1 in MDA-MB-231 and BT-549 spheroids treated with UA (20 μM) or PTX (20 μM) for 24 h was detected by western blotting. *P<0.05, **P<0.01 and ***P<0.001. Scale bar, 40 μm. UA, ursolic acid; ROS, reactive oxygen species; fer, ferrostatin-1; DFO, deferoxamine; MDA, malondialdehyde; TFR1, transferrin receptor 1; FTH1, ferritin heavy chain 1; NCOA4, nuclear receptor coactivator 4; FPN, ferroportin; PTX, paclitaxel; ns, not significant (P>0.05).

fer and DFO (Fig. 4B). Intracellular total iron and ferrous iron were significantly increased by UA treatment, and this increase was efficiently blocked by fer and DFO (Fig. 4C). Several key regulators of iron metabolism were therefore examined, including TFR1 for ferric iron uptake, FTH1 for ferrous iron storage, nuclear receptor coactivator 4 (NCOA4) for releasing ferrous iron in the lysosome, and FPN for iron export. The expression of TFR1, which was upregulated in BCSCs, was significantly decreased upon UA treatment as detected by RT-qPCR and WB (Fig. 4D and E). Fer and DFO efficiently reversed UA-induced TFR1 downregulation, indicating that TFR1 expression is mainly regulated by intracellular iron concentration (Fig. 4D). Consistent with the increase in ferrous iron in UA-treated BCSCs (Fig. 4C), FTH1 and NCOA4 were significantly enhanced upon UA treatment, and this was reversed by fer and DFO (Fig. 4D). FPN also increased prominently upon UA treatment and this was reversed by fer and DFO (Fig. 4D). Thus, UA-induced ferrous iron accumulation might be related to ferritin formation and degradation. These data indicated that UA might induce ferroptosis through stimulating ferrous iron and ROS accumulation in BCSCs.

UA regulates ferroptosis through the KEAP1-NRF2-mediated pathway in BCSCs. NRF2, the master regulator of the antioxidant system, is known to play a crucial role in the transcriptional regulation of ferroptosis by targeting FTH1, TFR1, FSP1, GPX4 and SLC7A11 (32). KEAP1 acts as a negative regulator of NRF2 through the ubiquitin-proteasome pathway. In the present study, it was observed that the expression of KEAP1 was enhanced by UA treatment and this was reversed by fer and DFO in MDA-MB-231 spheroids (Fig. 5A). Similarly, the total level of p-NRF2/NRF2 and p-NRF2/NRF2 in the nucleus was decreased by UA treatment as well, and this was reversed by fer and DFO (Fig. 5B and C). Thus, UA may induce ferroptosis through stabilizing KEAP1 and inhibiting NRF2 activation. The main ferroptosis-suppressing pathways were further investigated; namely the GSH/GPX4 pathway and the FSP1 pathway, which is GPX4 independent. As demonstrated in Fig. 5D and E, SLC7A11, GPX4 and FSP1 were significantly reduced upon UA treatment in MDA-MB-231 and BT-549 spheroids. Fer and DFO efficiently reversed the UA-induced decline of SLC7A11, GPX4 and FSP1. These results indicated that UA may induce ferroptosis through the KEAP-NRF2-mediated pathway.

UA inhibits proliferation of BCSCs in mouse xenograft models. A subcutaneous tumor model was established to study the therapeutic potential of UA *in vivo*, and tumor growth was observed periodically (Fig. 6A-C). It was found that compared with DMSO treatment, UA treatment significantly slowed tumor growth, which was significantly more efficient than PTX treatment. The inhibitory effects of UA were attenuated by fer and DFO. Furthermore, TFR1, KEAP1 and NRF2 expression levels were detected in tumor tissues. Consistent with WB analyses, the expression levels of TFR1 and NRF2 were declined, and KEAP1 was enhanced by UA treatment, which could be reversed by fer and DFO administration (Fig. 6D). The schematic model depicting how UA regulates the KEAP1/NRF2 pathway and ferroptosis is shown in Fig. 6E.

Discussion

Cancer heterogeneity stands as a primary factor behind drug resistance and tumor recurrence. Within cancer cells, CSCs represent a distinct subset intimately linked to therapeutic resistance. Prior investigations have pointed to iron dependency and ferroptosis dysregulation within CSCs (11). Notably, compared with non-CSCs, CSCs in breast cancer and glioblastoma exhibit higher expression of TFR (33). Concurrently, TF levels were found to be elevated in glioblastoma stem cells and circulating melanoma cells (34). Previous findings also indicated that CD44 plays a role in regulating iron endocytosis, thereby maintaining the mesenchymal state of cells (35). These insights underscore the enhanced iron uptake and trafficking observed in CSCs. Interestingly, despite heightened iron uptake, CSCs predominantly store iron in the ferric state (ferritin), exhibiting resistance to ferroptosis, possibly attributed to increased expression of antioxidants such as SLC7A11 and GSH (36).

In breast cancer cell spheroids and $CD44^+/CD24^-$ populations derived from TNBC cell lines MDA-MB-231 and BT-549, elevated expression of TFR1 and FTH1 was observed, along with reduced iron export marked by lower FPN expression. Additionally, spheroids and BCSCs exhibited iron accumulation primarily in the ferric form. Lipid peroxidation levels were diminished in spheroids and BCSCs, as evidenced by reduced levels of MDA. Furthermore, the levels of GSH, a crucial intracellular antioxidant, were significantly higher in spheroids and CSCs compared with adherent cells. Importantly, inhibitors of ferroptosis such as SLC7A11, GPX4 and NRF2 were significantly upregulated in spheroids and CSCs. In line with previous findings (33-35), the data of the present study confirmed that BCSCs exhibit enhanced iron accumulation and lower ferroptosis levels.

Given the heightened intracellular iron accumulation in CSCs, they become more susceptible to ferroptosis activators. Targeting ferroptosis has emerged as a promising strategy to address CSC-related tumor metastasis and drug resistance (16). Several studies have indicated that CSCs exhibit increased sensitivity to ferroptosis-inducing agents (11,36,37). In the present study, it was observed that TNBC spheroids were more prone to UA-induced cell death (Fig. 3A). Notably, ferroptosis inhibitors fer (which blocks lipid peroxidation) and DFO (an iron chelator) efficiently reversed UA-induced cell death. Furthermore, UA treatment led to a decrease in CD44 expression, an increase in CD24 expression, and downregulation of stemness regulators, which could be effectively attenuated by fer and DFO. The inhibitory effects of UA on BCSCs were further validated in xenografted mice. Collectively, these findings highlight UA as a potent ferroptosis inducer capable of efficiently inhibiting stemness characteristics and proliferation of BCSCs.

Furthermore, it was demonstrated that UA disrupts iron homeostasis, leading to intracellular ferrous iron and ROS accumulation. Several iron metabolism regulators were altered upon UA treatment. TFR1, which was upregulated in BCSCs, significantly decreased following UA treatment. Additionally, UA enhanced both ferritin formation, indicated by FTH1 expression, and degradation, indicated by NCOA4 expression. These observations suggested that UA may induce ferroptosis

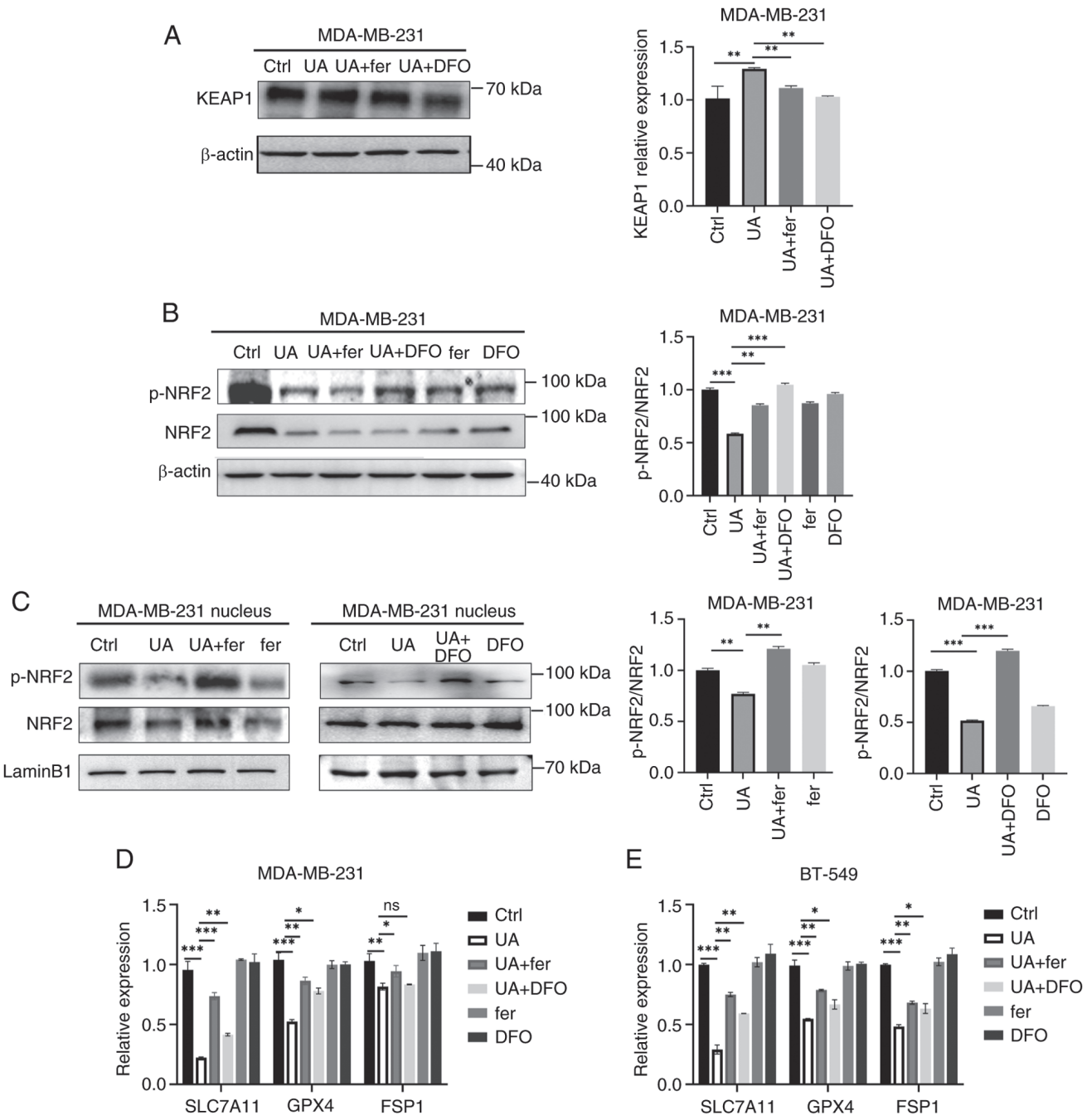

Figure 5. UA regulates ferroptosis through the KEAP1-NRF2-mediated pathway in breast cancer stem-like cells. (A) Protein expression levels of KEAP1 in MDA-MB-231 spheroids treated with UA (20 μM) together with or without ferroptosis inhibitors, fer (2 μM) and DFO (10 μM), were detected by western blotting for 48 h. (B) Total proteins and (C) nucleic proteins were collected from MDA-MB-231 spheroids after the same treatment as in panel B. p-NRF2 and NRF2 were detected by western blotting. (D and E) The mRNA levels of SLC7A11, GPX4 and FSP1 in MDA-MB-231 and BT-549 spheroids were analyzed by reverse transcription-quantitative PCR after the treatment of UA together with or without ferroptosis inhibitors for 48 h. *P<0.05, **P<0.01 and ***P<0.001. UA, ursolic acid; KEAP1, Kelch-like ECH-associated protein 1; NRF2, nuclear factor erythroid-related factor 2; fer, ferrostatin-1; DFO, deferoxamine; p-, phosphorylated; SLC7A11, solute carrier family 7 member 11; GPX4, glutathione peroxidase 4; FSP1, ferroptosis suppressor protein 1; ns, not significant (P>0.05).

through the alteration of iron homeostasis, resulting in the release of ferrous iron into the cytosol.

GSH, the most abundant reductant in mammalian cells, is synthesized from cystine, which is taken up by the system xc^- cystine/glutamate antiporter, a transmembrane protein complex containing subunits SLC7A11 and SLC3A2 (38). The SCL7A11-GSH-GPX4 axis has been demonstrated to play a crucial role in suppressing ferroptosis (10,39). GPX4 is the primary enzyme catalyzing the reduction of phospholipid hydroperoxides in mammalian cells, thereby preventing lipid peroxidation and ferroptosis. Previous genome-wide screenings have unveiled GPX4-independent mechanisms, such as the FSP1-CoQ10-NAD(P)H pathway, which inhibits ferroptosis independently of GPX4 (40,41). In investigating the pathway through which UA regulates ferroptosis, significant reductions in SLC7A11, GPX4 and FSP1 were observed upon UA treatment in spheroids. Notably, fer and DFO efficiently reversed the decline of SLC7A11, GPX4 and FSP1 induced by

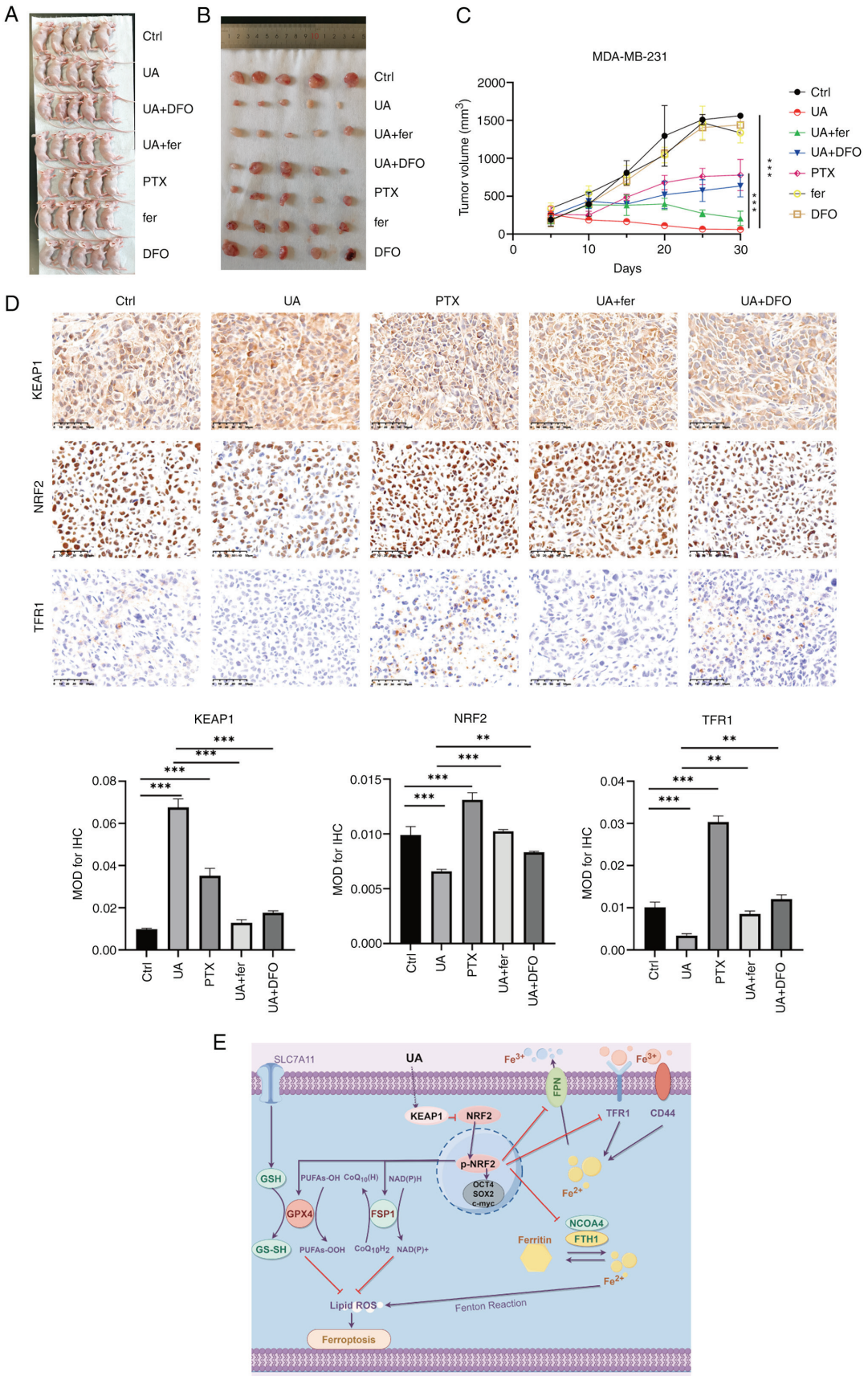

Figure 6. UA inhibits proliferation of breast cancer stem-like cells in mouse xenograft models. After the mouse xenograft model was established, the mice were injected with UA at 20 mg/kg daily, PTX at 20 mg/kg daily, DMSO at 20 mg/kg daily, fer at 5 mg/kg daily, and DFO at 100 mg/kg daily. (A) Images of the animals at the time of euthanasia. (B) Images of all the tumors excised from each animal. (C) Tumor volumes were measured every five days after subcutaneous injection of 5x106 MDA-MB-231 spheroids. (D) Immunohistochemical staining and mean optical density values of KEAP1, NRF2 and TFR1 in tumor tissues from xenografted mice with different treatments as indicated. (E) The schematic model depicting how UA regulates KEAP1/NRF2 pathway and ferroptosis drawn by Figdraw 2.0 (https://www.figdraw.com/static/index.html#/). **P<0.01 and ***P<0.001. Scale bar, 50 µm. UA, ursolic acid; PTX, paclitaxel; fer, ferrostatin-1; DFO, deferoxamine; KEAP1, Kelch-like ECH-associated protein 1; NRF2, nuclear factor erythroid-related factor 2; TFR1, transferrin receptor 1.

UA. These results suggested that UA-induced ferroptosis may be regulated through the SLC7A11/GPX4 and FSP1 pathway in an iron-dependent manner.

To further elucidate the mechanism by which UA induces ferroptosis, the key regulator of oxidative stress, KEAP1/NRF2, was investigated. KEAP1 acts as a negative regulator of NRF2 via the ubiquitin-proteasome pathway. NRF2 regulates the antioxidant system by transcriptionally regulating several key regulators involved in ferroptosis, including FTH1, TFR1, FSP1, GPX4 and SLC7A11 (32). It was observed that UA treatment enhanced the expression of KEAP1, which was reversed by fer and DFO in MDA-MB-231 spheroids and tissue samples from xenografted mice. Furthermore, p-NRF2 levels were significantly decreased following UA treatment in both MDA-MB-231 spheroids and tissue samples from xenografted mice. These findings suggested that UA may induce ferroptosis by stabilizing KEAP1 and inhibiting NRF2 activation.

Through utilization of spheroids and a xenografted mouse model, it was demonstrated that UA exhibits promising potential in inhibiting stemness and proliferation of BCSCs by inducing ferroptosis. These findings expand the scope of clinical application of UA and provide theoretical support for its use in the treatment of TNBC.

Acknowledgements

Not applicable.

Funding

The present study was supported by the National Natural Science Foundation of China (grant nos. 81972252, 81670573, 81830052 and 82127807), the Shanghai Nature Science Foundation (grant no. 22ZR1428000), the National Key Research and Development Program of China (grant no. 2020YFA0909000) and the Construction Project of Shanghai Key Laboratory of Molecular Imaging (grant no. 18DZ2260400).

Availability of data and materials

The data generated in the present study may be requested from the corresponding author.

Authors' contributions

XY, JZ and GH conceived and designed the study. XY, BL, LZ, MZ, MM and LQ collected and processed samples. XY, JZ, MM and HY performed data analysis and interpretation. BL, HY and JZ provided resources. XY, BL, HY, GH and JZ wrote and edited the manuscript. All authors read and approved the final manuscript. XY and JZ confirm the authenticity of all the raw data.

Ethics approval and consent to participate

Animal welfare and experimental procedures were performed strictly in accordance with high standards for animal welfare and other related ethical regulations approved by the Shanghai University of Traditional Chinese Medicine. All animal experiments were performed in compliance with the ARRIVE guidelines. The study was approved (approval no. 2022-SZR-18-45010319800509104X) by the Animal Ethics Committee of Shanghai University of Medicine and Health Sciences (Shanghai, China). All methods were carried out in accordance with relevant guidelines and regulations.

Patient consent for publication

Not applicable.

Competing interests

The authors declare that they have no competing interests.

References

1. Sung H, Ferlay J, Siegel RL, Laversanne M, Soerjomataram I, Jemal A and Bray F: Global cancer statistics 2020: Globocan estimates of incidence and mortality worldwide for 36 cancers in 185 countries. CA Cancer J Clin 71: 209-249, 2021.
2. Houghton SC and Hankinson SE: Cancer progress and priorities: Breast cancer. Cancer Epidemiol Biomarkers Prev 30: 822-844, 2021.
3. Deng H, Muthupalani S, Erdman S, Liu H, Niu Z, Wang TC and Fox JG: Translocation of Helicobacter hepaticus synergizes with myeloid-derived suppressor cells and contributes to breast carcinogenesis. Oncoimmunology 11: 2057399, 2022.
4. Sharma P: Biology and management of patients with triple-negative breast cancer. Oncologist 21: 1050-1062, 2016.
5. Hsu JY, Chang CJ and Cheng JS: Survival, treatment regimens and medical costs of women newly diagnosed with metastatic triple-negative breast cancer. Sci Rep 12: 729, 2022.
6. Thiagarajan PS, Sinyuk M, Turaga SM, Mulkearns-Hubert EE, Hale JS, Rao V, Demelash A, Saygin C, China A, Alban TJ, *et al*: Cx26 drives self-renewal in triple-negative breast cancer via interaction with NANOG and focal adhesion kinase. Nat Commun 9: 578, 2018.
7. Toledo-Guzmán ME, Bigoni-Ordóñez GD, Ibáñez Hernández M and Ortiz-Sánchez E: Cancer stem cell impact on clinical oncology. World J Stem Cells 10: 183-195, 2018.
8. Lin X, Wang Y, Fang K, Guo Z, Lin N and Li L: The application of nanoparticles in theranostic systems targeting breast cancer stem cells: Current progress and future challenges. Stem Cell Res Ther 14: 356, 2023.
9. Liu S, Cong Y, Wang D, Sun Y, Deng L, Liu Y, Martin-Trevino R, Shang L, McDermott SP, Landis MD, *et al*: Breast cancer stem cells transition between epithelial and mesenchymal states reflective of their normal counterparts. Stem Cell Reports 2: 78-91, 2013.
10. Jiang X, Stockwell BR and Conrad M: Ferroptosis: Mechanisms, biology and role in disease. Nat Rev Mol Cell Biol 22: 266-282, 2021.
11. Cosialls E, El Hage R, Dos Santos L, Gong C, Mehrpour M and Hamaï A: Ferroptosis: Cancer stem cells rely on iron until 'to die for' It. Cells 10: 2981, 2021.
12. Torti SV and Torti FM: Iron and cancer: More ore to be mined. Nat Rev Cancer 13: 342-355, 2013.
13. Mai TT, Hamaï A, Hienzsch A, Cañeque T, Müller S, Wicinski J, Cabaud O, Leroy C, David A, Acevedo V, *et al*: Salinomycin kills cancer stem cells by sequestering iron in lysosomes. Nat Chem 9: 1025-1033, 2017.
14. Pandrangi SL, Raju Bagadi SA, Sinha NK, Kumar M, Dada R, Lakhanpal M, Soni A, Malvia S, Simon S, Chintamani C, *et al*: Establishment and characterization of two primary breast cancer cell lines from young Indian breast cancer patients: Mutation analysis. Cancer Cell Int 14: 14, 2014.
15. Anandhan A, Dodson M, Schmidlin CJ, Liu P and Zhang DD: Breakdown of an ironclad defense system: The critical role of NRF2 in mediating ferroptosis. Cell Chem Biol 27: 436-447, 2020.
16. Sun S, Shen J, Jiang J, Wang F and Min J: Targeting ferroptosis opens new avenues for the development of novel therapeutics. Signal Transduct Target Ther 8: 372, 2023.
17. Zafar S, Khan K, Hafeez A, Irfan M, Armaghan M, Rahman AU, Gürer ES, Sharifi-Rad J, Butnariu M, Bagiu IC, *et al*: Ursolic acid: A natural modulator of signaling networks in different cancers. Cancer Cell Int 22: 399, 2022.

18. Zhang Y, Ma X, Li H, Zhuang J, Feng F, Liu L, Liu C and Sun C: Identifying the effect of ursolic acid against triple-negative breast cancer: Coupling network pharmacology with experiments verification. Front Pharmaco 12: 685773, 2021.
19. Zong L, Cheng G, Zhao J, Zhuang X, Zheng Z, Liu Z and Song F: Inhibitory effect of ursolic acid on the migration and invasion of doxorubicin-resistant breast cancer. Molecules 27: 1282, 2022.
20. Mandal S, Gamit N, Varier L, Dharmarajan A and Warrier S: Inhibition of breast cancer stem-like cells by a triterpenoid, ursolic acid, via activation of Wnt antagonist, sFRP4 and suppression of miRNA-499a-5p. Life Sci 265: 118854, 2021.
21. Li H, Yu Y, Liu Y, Luo Z, Law BYK, Zheng Y, Huang X and Li W: Ursolic acid enhances the antitumor effects of sorafenib associated with Mcl-1-related apoptosis and SLC7A11-dependent ferroptosis in human cancer. Pharmacol Res 182: 106306, 2022.
22. Workman P, Aboagye EO, Balkwill F, Balmain A, Bruder G, Chaplin DJ, Double JA, Everitt J, Farningham DAH, Glennie MJ, *et al*: Guidelines for the welfare and use of animals in cancer research. Br J Cancer 102: 1555-1577, 2010.
23. Stevens MF, Hickman JA, Langdon SP, Chubb D, Vickers L, Stone R, Baig G, Goddard C, Gibson NW, Slack JA, *et al*: Antitumor activity and pharmacokinetics in mice of 8-carbam oyl-3-methyl-imidazo[5,1-d]-1,2,3,5-tetrazin-4(3H)-one (CCRG 81045; M & B 39831), a novel drug with potential as an alternative to dacarbazine. Cancer Res 47: 5846-5852, 1987.
24. Yates AG, Weglinski CM, Ying Y, Dunstan IK, Strekalova T and Anthony DC: Nafamostat reduces systemic inflammation in TLR7-mediated virus-like illness. J Neuroinflammation 19: 8, 2022.
25. Sun N, Zhang RX, Wang Y, Huang ZJ, Han J, Bao YS, Duan WY, Dong CR, Deng GS and Zhuang G: Effects of ursolic acid on oxidative stress and inflammatory factors in a rat model of AR after PM2.5 exposure. Zhonghua Er Bi Yan Hou Tou Jing Wai Ke Za Zhi 57: 860-867, 2022 (In Chinese).
26. Innocenti F, Danesi R, Di Paolo A, Agen C, Nardini D, Bocci G and Del Tacca M: Plasma and tissue disposition of paclitaxel (taxol) after intraperitoneal administration in mice. Drug Metab Dispos 23: 713-717, 1995.
27. Dixon SJ, Lemberg KM, Lamprecht MR, Skouta R, Zaitsev EM, Gleason CE, Patel DN, Bauer AJ, Cantley AM, Yang WS, *et al*: Ferroptosis: An iron-dependent form of nonapoptotic cell death. Cell 149: 1060-1072, 2012.
28. Tang G, Chen Y, Chen J, Chen Z and Jiang W: Deferoxamine ameliorates compressed spinal cord injury by promoting neovascularization in rats. J Mol Neurosci 70: 1437-1444, 2020.
29. Ponti D, Costa A, Zaffaroni N, Pratesi G, Petrangolini G, Coradini D, Pilotti S, Pierotti MA and Daidone MG: Isolation and in vitro propagation of tumorigenic breast cancer cells with stem/progenitor cell properties. Cancer Res 65: 5506-5511, 2005.
30. Zhong Y, Shen S, Zhou Y, Mao F, Guan J, Lin Y, Xu Y and Sun Q: ALDH1 is a better clinical indicator for relapse of invasive ductal breast cancer than the CD44+/CD24-phenotype. Med Oncol 31: 864, 2014.
31. Sandhu SS, Rouz SK, Kumar S, Swamy N, Deshmukh L, Hussain A, Haque S and Tuli HS: Ursolic acid: A pentacyclic triterpenoid that exhibits anticancer therapeutic potential by modulating multiple oncogenic targets. Biotechnol Genet Eng Rev 4: 1-31, 2023.
32. Lee J and Hyun DH: The interplay between intracellular iron homeostasis and neuroinflammation in neurodegenerative diseases. Antioxidants (Basel) 12: 918, 2023.
33. Schonberg DL, Miller TE, Wu Q, Flavahan WA, Das NK, Hale JS, Hubert CG, Mack SC, Jarrar AM, Karl RT, *et al*: Preferential iron trafficking characterizes glioblastoma stem-like cells. Cancer Cel 28: 441-455, 2015.
34. Hong X, Roh W, Sullivan RJ, Wong KHK, Wittner BS, Guo H, Dubash TD, Sade-Feldman M, Wesley B, Horwitz E, *et al*: The lipogenic regulator SREBP2 induces transferrin in circulating melanoma cells and suppresses ferroptosis. Cancer Discov 11: 678-695, 2021.
35. Müller S, Sindikubwabo F, Cañeque T, Lafon A, Versini A, Lombard B, Loew D, Wu TD, Ginestier C, Charafe-Jauffret E, *et al*: CD44 regulates epigenetic plasticity by mediating iron endocytosis. Nat Chem 12: 929-938, 2020.
36. Pandrangi SL, Chittineedi P, Chalumuri SS, Meena AS, Neira Mosquera JA, Sánchez Llaguno SN, Pamuru RR, Mohiddin GJ and Mohammad A: Role of intracellular iron in switching apoptosis to ferroptosis to target therapy-resistant cancer stem cells. Molecules 27: 3011, 2022.
37. Doll S, Proneth B, Tyurina YY, Panzilius E, Kobayashi S, Ingold I, Irmler M, Beckers J, Aichler M, Walch A, *et al*: ACSL4 dictates ferroptosis sensitivity by shaping cellular lipid composition. Nat Chem Biol 13: 91-98, 2017.
38. Koppula P, Zhuang L and Gan B: Cystine transporter SLC7A11/xCT in cancer: Ferroptosis, nutrient dependency, and cancer therapy. Protein Cell 12: 599-620, 2021.
39. Yang WS, SriRamaratnam R, Welsch ME, Shimada K, Skouta R, Viswanathan VS, Cheah JH, Clemons PA, Shamji AF, Clish CB, *et al*: Regulation of ferroptotic cancer cell death by GPX4. Cell 156: 317-331, 2014.
40. Doll S, Freitas FP, Shah R, Aldrovandi M, da Silva MC, Ingold I, Goya Grocin A, Xavier da Silva TN, Panzilius E, Scheel CH, *et al*: FSP1 is a glutathione-independent ferroptosis suppressor. Nature 575: 693-698, 2019.
41. Bersuker K, Hendricks JM, Li Z, Magtanong L, Ford B, Tang PH, Roberts MA, Tong B, Maimone TJ, Zoncu R, *et al*: The CoQ oxidoreductase FSP1 acts parallel to GPX4 to inhibit ferroptosis. Nature 575: 688-692, 2019.